Nanoscale

PAPER

View Article Online
View Journal | View Issue

Cite this: *Nanoscale*, 2019, **11**, 21872

Boosting the analytical properties of gold nanostars by single particle confinement into yolk porous silica shells†

Maria Blanco-Formoso,‡[a,b] Ana Sousa-Castillo,‡[a] Xiaofei Xiao,[c,d] Andrea Mariño-Lopez,[a] Mariacristina Turino,[b] Nicolas Pazos-Perez,[b] Vincenzo Giannini,*[c,d] Miguel A. Correa-Duarte*[a] and Ramon A. Alvarez-Puebla *[b,e]

Received 12th September 2019,
Accepted 29th October 2019

DOI: 10.1039/c9nr07889d

rsc.li/nanoscale

Herein we illustrate an effective protocol to boost the optical enhancing properties of gold nanostars. By coating single nanostars with a mesoporous silica layer of the appropriate size (yolk capsules), to localize them under optical microscopy, it is possible to enumerate single particles and design SERS quantitative methods with minute amounts of metallic particles.

Introduction

Gold nanostars (NSts) are among the most efficient particles in nanophotonics. The particular shape of these star-shaped colloids allows for the concentration of extraordinarily high electromagnetic fields at their tips.[1] This, combined with the conventional position of their localized surface plasmon resonances (LSPRs) in the near infrared (NIR) region, permits their use in a myriad of different photonic applications. For example, gold nanostars have been successfully used in technological applications such as the generation of three-photon photoemission under continuous-wave illumination,[2] lasing[3] or the fabrication of organic light-emitting diodes[4] and solar cells.[5] On the other hand, these nanostructures are widely used in biology and nanomedicine due to the fact that they are biocompatible,[6] can be easily internalized in cells[7] and tissues[8] and present LSPRs inside the biological window.[9] In this regard, NSts are commonly employed not only in photothermal therapy[10,11] and photothermal drug delivery[12,13] but also in biological and medical imaging.[14,15] Furthermore, the efficient generation of intense electromagnetic fields in NSts is commonly exploited in plasmon-assisted spectroscopy for the design of ultrasensitive sensors.[16] NSts have been exploited as direct sensing elements through LSPR shifting[17,18] or as platforms for metal enhanced fluorescence;[19,20] although, indeed, their most prolific applications are those derived from their use as substrates for surface-enhanced Raman scattering (SERS) spectroscopy.[21]

Gold nanostars are among the very few substrates capable of single-particle ultrasensitive spectroscopy.[22,23] However, and in contrast to other substrates in which the SERS intensity increases with the concentration of nanoparticles by the formation of hot spots, in NSts the intensity decreases with the particle concentration as previously demonstrated.[24] This experimental fact had been explained as inefficient formation of hot spots due to the symmetry mismatch as a consequence of the complex shape of these particles.[24,25] Thus, to solve this situation, many groups have reported procedures to coat the nanostars with different porous materials including silica[26] and polymers,[25] thus looking for the isolation of the plasmonic core while allowing for small molecules to diffuse inside. Other approaches to profit from the exceptional optical properties of these structures rely on their use as encoded particles, where the plasmonic core is conjugated with a SERS label and isolated through silica,[27] polymeric shell[28] or metal organic frames[13,16] from the exterior. These approaches, however, notably restrict the availability of the plasmonic surfaces limiting their capacity to interact with the target analytes.

Herein, we engineer a new strategy to boost the analytical properties of nanostars based on the confinement of single plasmonic particles in the yolk shells of mesoporous silica. In

[a]*Department of Physical Chemistry, Singular Center for Biomedical Research (CINBIO), Southern Galicia Institute of Health Research (IISGS) and Biomedical Research Networking Center for Mental Health (CIBERSAM), Universidade de Vigo, 36310 Vigo, Spain. E-mail: macorrea@uvigo.es*
[b]*Department of Physical Chemistry and EMaS, Universitat Rovira i Virgili, 43007 Tarragona, Spain. E-mail: ramon.alvarez@urv.cat*
[c]*The Blackett Laboratory, Imperial College London, London SW7 2AZ, UK*
[d]*Instituto de Estructura de la Materia (IEM-CSIC), Consejo Superior de Investigaciones Cientificas, Serrano 121, 28006 Madrid, Spain. E-mail: v.giannini@csic.es*
[e]*ICREA, Passeig Lluis Companys 23, 08010 Barcelona, Spain*

†Electronic supplementary information (ESI) available: Statistical data of the nanostar geometry. Additional TEM images and electric near-field intensity maps. See DOI: 10.1039/c9nr07889d

‡These authors contributed equally to this work.

this configuration, the NSt can be cleaned of spurious surfactants on their surface, are free to interact with the surrounding media and are protected from plasmonic coupling between themselves. Additionally, this configuration also allows the fine monitoring of the number of scatterings as they are visible (and can be enumerated) through the standard confocal optical microscope commonly attached to the Raman system.

Results and discussion

Fig. 1A and B show the representative images of 60 nm-sized gold nanospheres, synthesized through a kinetically controlled seed-mediated growth,[29] and the corresponding nanostars (~110 nm, Fig. 1A and S1†).[2] The particles are characterized by major plasmonic resonances centered at 552 and 779 nm for spheres and stars, respectively (Fig. 1C). To test their optical enhancing properties, solutions of 10^{-3} M were mixed with benzenethiol (BT) to reach the final concentration of 10^{-5} M. BT was selected as the optical probe as it presents its HOMO–LUMO transition, far way in the ultraviolet region, which allows for the isolation of the enhancement factor as purely electromagnetic with no contributions of chemical effects or resonance Raman spectroscopy. Finally, by using a thiol we ensure a high affinity towards the gold surfaces and thus the possibility of quantifying the amount of molecules was retained on the surfaces in each experiment. Note that this concentration was selected to ensure the formation of a compact monolayer of the analyte through the nanoparticle surfaces. Then the samples were directly cast, to generate aggregated films, or spin-coated, to generate isolated nanoparticles, on glass slides. These films were then mapped with a 785 nm laser line through a 100× microscope objective. Fig. 1D and E show the SERS spectra and the corresponding average intensities of BT on different films. Fig. 1F–I show the particle density (SEM), morphology (SEM and optical micrographs) and the intensity distribution (SERS images) of each film. Notably, the characteristic SERS spectrum of BT[30] can be appreciated in all the samples except for that of the isolated spheres. Consistent with previous reports,[31] this absence of signal is interpreted as the lack of electromagnetic field in the single isolated spherical particles to generate enough SERS signal. Conversely, when the spheres aggregate, the signal increases mainly due to the formation of hot spots.[32] In contrast, isolated nanostars give rise to an intense neat and clear spectrum of BT; however, when aggregated, intensity substantially decreases. It is important to note that although for all the prepared samples the best SERS intensity comes from the aggregated spheres, the signal of single nanostars is close to half of that of the aggregated films and present a much lower standard deviation.

To further understand the optical behavior of nanostars, the electric fields of interacting particles were simulated. In the nanostars, the number of configurations leading to exceptionally efficient hotspots may increase due to their complex morphology involved. Thus, for simplicity, gold nanostars were simulated as one spherical core with one tip either alone or interacting in different configurations with other nanostars. Fig. 2 shows the near-field maps at 785 nm (excitation light in our experiments). For excitation at 785 nm, single nanostars show intense localization of the electric field at the tip. However, when two nanostars interact, no matter the geometry, the electric field at the tip (normalized for one star) decreases mainly due to a red shift of the computed LSPR.

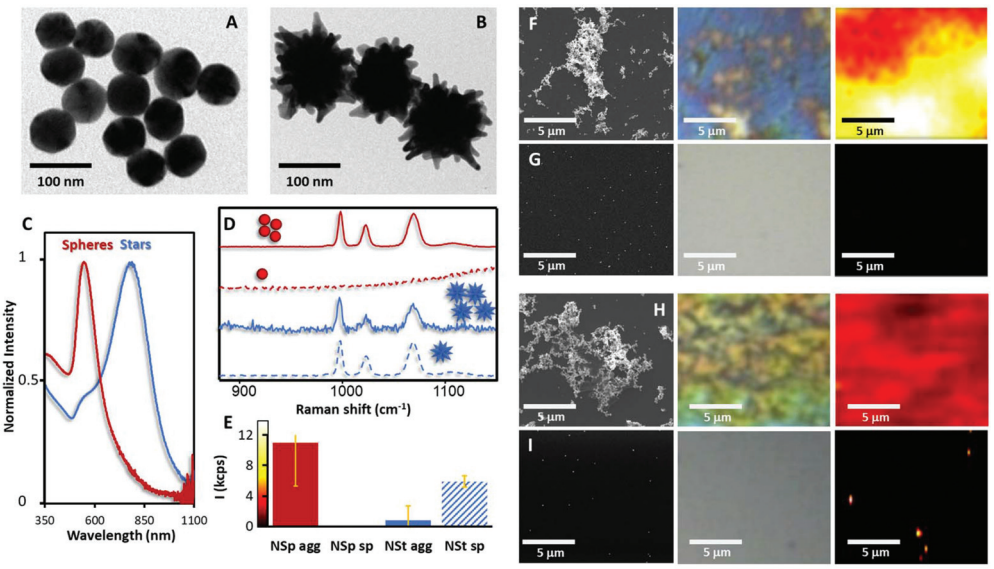

Fig. 1 TEM images of (A) spherical gold colloids of 60 nm in diameter used as seeds to produce (B) gold nanostars of 100 nm. (C) Characteristic LSPR spherical particles and nanostars. (D) SERS spectra and (E) average intensity of benzenethiol on different experiments (F–I). SEM (left), confocal optical (center) and SERS (right, color scale is shown in the *y*-axis of (E)) images of films prepared with nanospheres (F) aggregated and (G) with isolated, or with nanostars (H) aggregated and (I) isolated.

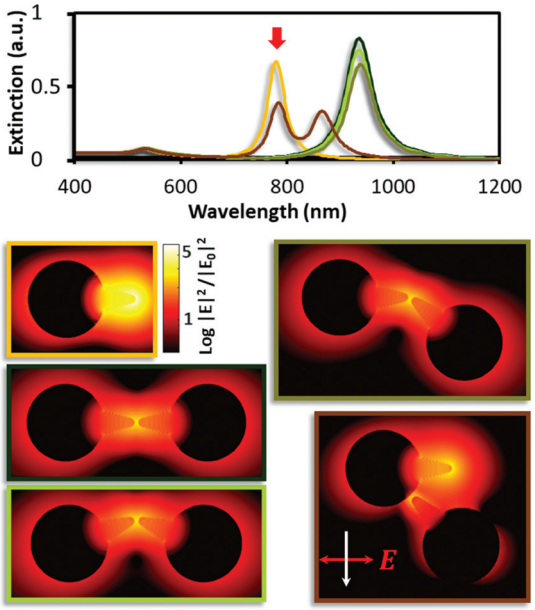

Fig. 2 FDTD calculations of the extinction spectra of a NSt isolated and interacting in different configurations (tip to tip at different angles and tip to core) and the electric near-field intensity maps for each configuration upon excitation at 785 nm. Note that the results are normalized to one star.

This is corroborated by the excitation of each of the configurations at their maximum extinction, respectively, (Fig. S2†) where a slight increase of the fields can be observed in perfectly aligned interacting tips which slightly decreases as they form an angle. Furthermore, the interaction of the tip of one star with the core of another star results in both, the decrease in the field of both tips and the red shift of the field of the interacting tip. These calculations strongly suggest, in a certain manner, a similar behavior of the nanostars related to that of the other nanoparticle shapes. While in nanospheres, aggregation leads to the random formation of hot spots and the subsequent red shift of the global plasmon, thus improving the coupling with 785 nm light; in nanostars, the red shift due to the random interaction moves away the LSPR hindering the plasmon coupling with the 785 nm light. Accordingly, as commercial Raman microscopes are equipped with standard laser lines in the green (514 or 532 nm), red (633 nm) and NIR (785 nm) regions, nanostar aggregation leads to a loss of analytical potential as compared with the use of single isolated nanoparticles.

As an alternative to the use of bare or polymer protected AuNSts, these particles can be isolated and placed into a submicrometer mesoporous silica shell forming a yolk particle. A simple strategy to create this kind of yolk–shell particle relies on the coating of the nanoparticles with organic sacrificial layers of polymers or surfactants which are removed after the formation of the silica shell.[33–35] This method of production, however, requires time and does not produce high yields. Also, these shells lead however to shells with small free inner volume, which is not appropriate for effective solvent exchange through the mesoporous silica.[33,34] Alternatively, in order to obtain large shells confining single particles, the gold nanospheres can be added directly to a polystyrene (PS) emulsion reactor, which yields homogeneous PS beads (Fig. S3A†). Notably within this method, besides the ratio styrene : nanoparticle, optimized to 140 mL of styrene per mL of 60 nm nanospheres (1.59 M in Au), the most important factor to obtain shells with single particles is related to the time of addition of the gold nanospheres, set, in our case, to five minutes after the beginning of the polymerization. If the gold nanoparticles are added before the starting of the polymerization, they aggregate generating heterogeneous PS beads containing nanoparticle agglomerates (Fig. S3B†). Nanoparticle additions after the optimized time produce also heterogeneous beads containing more than one nanoparticle per bead (Fig. S3C†). Conversely, by adding the initial gold spherical seeds at the appropriate time, it is possible to achieve homogeneous PS beads each containing a single gold nanosphere with yields above 90% (Fig. 3A). The beads can then be coated with mesoporous silica[36,37] (Fig. 3B) and the polystyrene core can be removed. This last step can be accomplished either by solvent dissolution of PS[38] or by combustion (Fig. 3B). In this case, we chose the second alternative (600 °C for 6 h) as it leads to a cleaner material while hardens the silica, and devel-

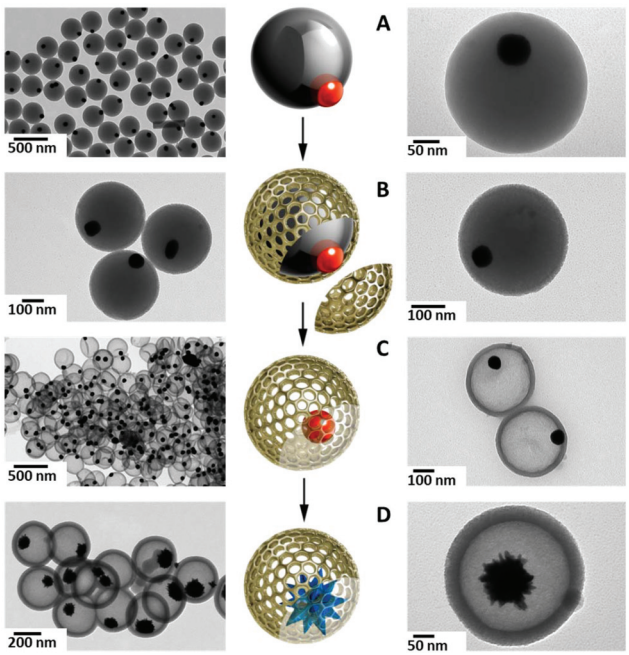

Fig. 3 Scheme and TEM images of the protocol for the preparation of single star yolk shells. Firstly, spherical nanoparticles are added to an emulsion polymerization reactor after the beginning of the reaction. (A) This yields particles composed of a single gold colloid entrapped in a homogeneous polystyrene bead. (B) Then, the beads can be coated with a mesoporous coating of silica which, lastly, (C) is calcined. The calcination stabilizes the silica, develops the porosity and degrades the polymer generating the yolk shell. (D) The spherical nanoparticles can be then overgrown to nanostars.

ops and stabilizes the porosity[39,40] and confers colloidal stability to the yolk shells in aqueous solution (Fig. 3C).[41] However, this step should be performed carefully as inappropriate conditions of temperature and/or time may lead to shell rupture (Fig. S4†). Finally, nanospheres were grown into nanostars inside the shell by using the standard DMF/PVP method.[2,42,43] In these particles, as water stability is mainly attained by the silica shell,[33] extensive cleaning of the nanoparticles can be achieved giving rise to appropriately optimized plasmonic material for optical sensing (Fig. 3C). Note that this fabrication protocol can be extended to other particle sizes and shapes by just slightly tuning the method. For example, smaller nanostars, obtained with 20 nm gold nanospheres are shown in Fig. S5.† Also, the direct inclusion of Au nanostars into the polymer core was performed. This approach, however, has several disadvantages. Firstly, the thermal treatment to remove the polymer may lead to reshaping of the stars. Additionally, if the polymer is removed with solvents, part of the polymeric material may remain on the plasmonic surface passivating them.

The yolk confined nanostars ($NSt@SiO_2$) present similar optical properties to those uncoated. Fig. 4A shows how the LSPR redshifts from the red to the infrared region when the tips are grown on spherical particles either uncoated in solution (dotted lines) or inside the yolk shells. To test the optical enhancing properties of these capsules, samples were incubated with benzenethiol 10^{-5} M to ensure full coating of all the surfaces; then, films were prepared either by casting and air-drying of a concentrated solution of yolk shells to obtain aggregates ($NSt@SiO_2$ agg, Fig. 4B) or by spin-coating of diluted solutions to obtain single isolated capsules (Fig. 4C). Both films were then imaged with a NIR laser to achieve the SERS efficiencies ($NSt@SiO_2$ sp, Fig. 4D). Unlike the case of uncoated NSts, no matter the aggregation degree, both samples showed strong SERS intensity, indicating that BT was able to diffuse freely through the pores of the yolk shell[36] and that this shell was isolating the stars from the plasmonic coupling with other neighboring particles. Furthermore, although individual capsules can be identified by SEM in both films, optical microscopy can only discriminate individual particles when they are isolated in the spin-coated films (see the second panel of Fig. 4C). Thus, while SERS intensities provided by the aggregates may be larger, quantification of the number of capsules providing the signal is impossible. Conversely, with the sample composed of isolated $NSt@SiO_2$, the number of capsules sampled is known and the total intensity can be normalized to a single particle and thus can provide a robust plasmonic substrate for quantitative applications.

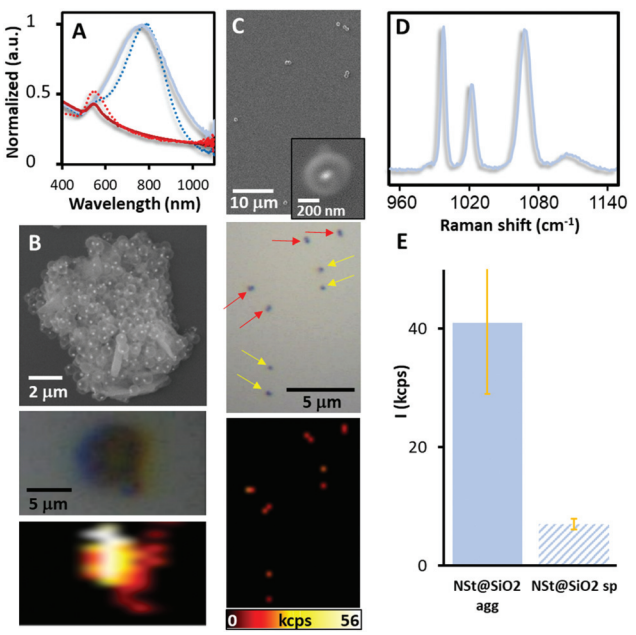

Fig. 4 (A) LSPRs of uncoated (dotted lines) and yolk-coated gold nanospheres (red) and nanostars (blue). (B) SEM, confocal optical image and SERS mapping of an aggregate of yolk-coated single nanostars prepared by casting and air-drying a concentrated solution of NSTs incubated with benzenethiol overnight. (C) SEM, confocal optical image and SERS mapping of an aggregate of yolk-coated single nanostars prepared by spin-coating a diluted solution of NSTs incubated with benzenethiol overnight. Note that the arrows in the optical image mark single capsules (yellow) and capsule dimers (red). (D) Representative SERS spectrum of BT and (E) the corresponding SERS intensities for aggregated and isolated single nanostar yolk shells.

Bearing in mind the above statement, an experiment was performed with a constant concentration of capsules (2×10^{-3} M in gold; 2.26×10^7 capsules per µL) incubated overnight with different concentrations of BT (from 10^{-5} to 10^{-13} M) and spin-coated (after dilution) to form isolated capsule films (Fig. 5). The SERS examination of these films by using a NIR laser and a 50× objective yielded strong SERS signals for individual particles until reaching BT concentrations in the nanomolar regime. From this point onwards, BT signals were only obtained on capsule aggregates. By estimating the surface area per nanostar as a sphere exceeding 50% the average length of the tips, it is possible to approximate the number of molecules per particle ($4.52\ 10^4$ nm^2), and assuming the surface area of a BT compact monolayer as 0.3 nm^2,[44] it is possible to estimate the number of BT molecules adsorbed on each single capsule (Table 1).

According to this approach, and assuming a complete reaction of BT with gold, a full monolayer of BT is achieved only at 10^{-5} M. From 10^{-6} to 10^{-10} M, NSts are coated with a BT submonolayer, while from 10^{-10} M onwards only one or less molecules are present on each star. Thus, in full agreement with the above description, an individual yolk capsule can enhance the signal of minute amounts of analyte (tens of molecules), while for further sensitivity (*i.e.*, less analyte concentration), aggregates composed of many capsules are required. This is also observed in the representation of the SERS intensity *versus* the concentration which shows an S-shaped curve implying a quantitative regime only between moderate to low quantities of the analyte, in the micro to nanomolar regimes. Ultrasmall traces of the analyte can also be determined but not quantitatively as the enumeration of yolk capsules in an aggregate is impossible with confocal microscopy.

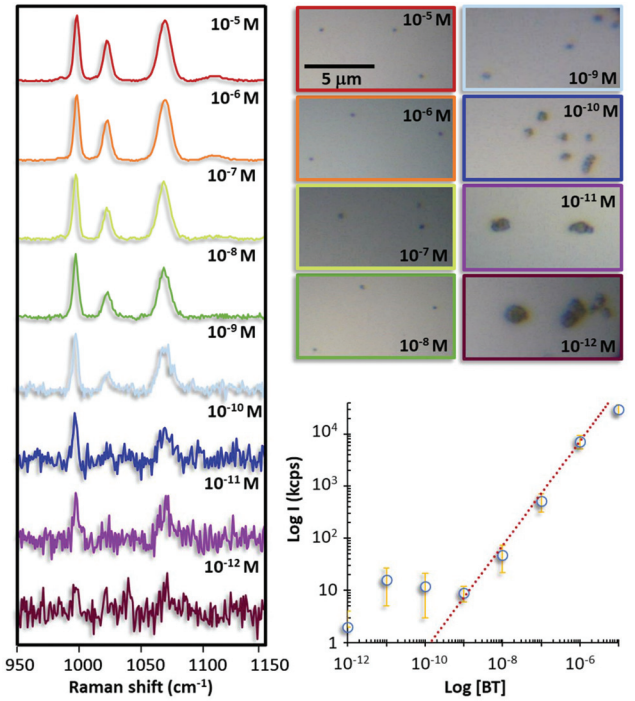

Fig. 5 SERS spectra recorded on spin-coated films after incubation with BT at different concentrations. Confocal optical images of the spectra recorded and comparison of the SERS intensity as a function of the analyte concentration.

Table 1 Number of BT molecules available per volume, area, and nanoparticle. Showing also when the NP surface is saturated, and the excess of BT remains in solution

$[BT]_{final}$	BT molecules/μl	Ads BT molecules/NSt	Free BT molecules
10^{-5}	6×10^{12}	1.5×10^{5}	1.16×10^{5}
10^{-6}	6×10^{11}	2.73×10^{4}	
10^{-7}	6×10^{10}	2.73×10^{3}	
10^{-8}	6×10^{9}	2.73×10^{2}	
10^{-9}	6×10^{8}	2.70×10^{1}	
10^{-10}	6×10^{7}	2.70	
10^{-11}	6×10^{6}	2.70×10^{-1}	
10^{-12}	6×10^{5}	2.70×10^{-2}	
10^{-13}	6×10^{4}	2.70×10^{-3}	

Conclusions

In summary, we illustrate here an effective protocol to boost the optical enhancing properties of gold nanostars. By placing single nanostars in the interior of mesoporous silica shells of the appropriate size (yolk capsules), it is possible to isolate their electromagnetic field avoiding the red-shift produced by the plasmonic interaction in between stars which leads to a consistent drop of signal in nanostar aggregates due to the loss of resonance with the incident laser. Furthermore, due to the sub-micrometric size of the yolk shells, the nanostars can be localized and enumerated with an optical microscope. This paves the way to the generation of new SERS quantitative methods with minute amounts of metallic particles. On the other hand, these yolk shells act as molecular sieves which also enhance the optical properties of the star as it restricts the contact of the plasmonic material with spurious large molecules present in all real fluids, either environmental or biological. Furthermore, the large steric and colloidal stabilization obtained with the coating avoids aggregation and facilitates the washing of metallic surfaces enabling their reaction with the analytes.

Experimental

Materials

Tetrachloroauric acid (99.9%), ammonium hydroxide solution (NH_4OH, 28–30%), trisodium citrate dehydrated (≥99.5%), sodium lauryl sulfate (99%), potassium persulfate (99%), styrene (99%), tetraethylorthosilicate (TEOS, 98%), cetyltrimethyl ammonium bromide (CTAB, 96%), *N*,*N*-dimethylformamide (DMF, 99.8%), polyvinylpyrrolidone (PVP, MW: 10 000), benzene thiol (BT), and ethanol (EtOH, absolute, ≥99.9%) were purchased from Sigma-Aldrich. All chemicals were of analytical grade and used without further purification. Milli-Q water (18 MΩ cm^{-1}) was used in all aqueous solutions, and all the glassware was cleaned with aqua regia before use.

Synthesis of 20 and 60 nm Au nanoparticles

Citrate-stabilized gold nanoparticles of 20 nm were prepared according to the well-known Turkevich method.[45] Briefly, a flask containing Milli-Q water (250 mL) was heated to 100 °C. After boiling had commenced, a solution of sodium citrate (5.5 mL, 0.1 M) was added to achieve the final citrate concentration of 2.2 mM. Boiling was continued for 1 min under vigorous stirring. Then, 0.416 mL of an aqueous solution of $HAuCl_4$ (0.1 M) were injected to the boiling solution. Boiling and stirring were continued for 30 min. A condenser was utilized to prevent the evaporation of the solvent. During this time, the color of the solution gradually changed from colorless to purple becoming, finally, red. The obtained nanoparticles have an average size of 21 ± 2 nm.

Alternatively, 60 nm-sized gold nanoparticles were synthesized following a kinetically controlled seed-mediated growth strategy.[29] First, Au NPs of 20 nm were produced as previously described. Immediately after the synthesis of the 20 nm Au seeds, the reaction was cooled to 90 °C. Then, 5 mL of $HAuCl_4$ (25 mM) were sequentially injected with a 30 min delay (1.67 mL each addition). After 30 min of the second addition, the first growth step is completed. After that, 90 mL of the sample were collected and diluted with 86.7 mL of water and 3.3 mL of sodium citrate (60 mM). This colloidal suspension was used as a seed solution by proceeding in the same way as for the first step (3 additions of 1.67 mL $HAuCl_4$ (25 mM) with a 30 min delay between each addition). By repeating this process several times (four steps), gold particles with an average diameter of 60 ± 3 nm were obtained. Both colloidal solutions were extensively cleaned and concentrated by

centrifugation (7000 rpm, 60 min and 4500 rpm, 30 min) to 30 mL and 135 mL, respectively. The final [Au^0] was 1.12 mM for the 20 nm Au NPs and 1.59 mM for the 60 nm Au NPs.

Near field enhancement calculations

The 3D numerical simulations were carried out using a finite-difference time-domain method (Lumerical FDTD Solutions).

In these simulations, the incident waves were directed onto the nanostructures with polarization along the dimer axis, as shown in the near field plots. To obtain the field enhancement shown in Fig. 2 or S2,† we used incident light with different wavelengths (785 nm, 935 nm, 938 nm, 784 nm, and 866 nm, respectively). In all simulations, the diameter of spheres was 50 nm.

The mesh size was set to 0.5 nm around the structures. A perfectly matched layer was applied in all directions.

Extinction spectra for nanostars were obtained by extrapolating to 6 tips the calculated result for a particle with a single tip by using the following relation: $\sigma_{sph} + 6(\sigma_{tip} - \sigma_{sph})$, where σ_{sph} is the extinction of a gold sphere with the same diameter as the core in the nanostar, and $\sigma_{1\text{-tip}}$ is the averaged spectrum for a single-tip particle.[23]

Synthesis of Au–PS composites

In the first step, sodium lauryl sulfate (0.028 g) was dissolved in a mixture of 25 mL of ethanol and 3 mL of water. Then, the solution was heated to 70 °C under a nitrogen flow, and 3 mL of potassium persulfate (0.03 M) were added. Subsequently, 420 μL of styrene were injected under magnetic stirring. After 5 minutes, 3 mL of each of the previously synthesized gold nanoparticles were slowly added, and the reaction was kept under stirring for 8 hours. Finally, the as-synthesized Au–PS composites were collected *via* centrifugation (6000 rpm, 20 min) and washed several times with ethanol. The obtained polystyrene spheres exhibited an average size of 450 nm.

Mesoporous silica coating and formation of the yolk–shell nanostructures

First, a SiO_2 shell was grown on top of the Au–PS composites using a modification of the well-known Stöber method.[46] More concretely, 12.5 mL of the Au–PS composite dispersion (1 mg mL^{-1}) were added to a mixture containing water (125 mL), ethanol (50 mL), and ammonia (1.5 mL). The mixture was sonicated for 10 min and, tetraethylorthosilicate ethanolic solution (5% v/v, 2.06 mL) was added dropwise. The mixture was mechanically stirred for 48 h. The excess of reagents was removed by three centrifugation–redispersion cycles with ethanolic solution (4500 rpm, 30 min). Yolk–shell silica microcapsules were obtained by calcination of PS present in the composites, at 600 °C for 6 h. The final powder was dispersed in 10 mL of ethanol.

Solvent transfer of Au nanoparticles

The aqueous dispersed spherical Au NPs were transferred to EtOH using PVP as a phase transfer agent. To do that, 3 mL of each of the Au nanoparticle solutions (20 and 60 nm) were added drop by drop under stirring to a previously sonicated (30 min) aqueous PVP solution (5 mL, 0.27 mM) and kept under stirring for 24 h at room temperature. Finally, the Au NPs were centrifuged (9000 rpm, 60 min and 7000 rpm, 35 min) and redispersed again in 3 mL (EtOH).

Synthesis of Au nanostars

Four different batches of Au nanostars were prepared using the previously produced Au nanoparticles as seeds (20 and 60 nm).[2,42,43] Two of them were prepared using the PVP capped AuNPs in EtOH, and the other two were prepared using the yolk–shell silica encapsulated ones. The nanostar growth was achieved by dissolving 1.5 g of PVP in DMF (15 mL). After its complete dissolution, the mixture was further sonicated for 30 min. Next, 1 mL of the Au seeds (either PVP coated or yolk–shell) was added and stirred for 2 h. Finally, an aqueous solution of $HAuCl_4$ (30 μl, 0.1.038 M) was injected under rapid stirring at room temperature. Within 15 min, the color of the solution changed from pink to blue, indicating the formation of Au nanostars. The solution was left under stirring overnight to ensure the reduction of all reactants. DMF and excess of PVP were removed by several centrifugation steps, a first one at 7500 rpm for 40 min, followed by two more at 7000 rpm for 10 min; in all the steps the particles were resuspended in EtOH (35 mL).

NP substrate deposition

All NPs (with and without the silica yolk–shell) were extra cleaned by four centrifugation steps (7000 rpm, 10 min) and resuspended in EtOH to achieve the final Au^0 concentrations of 2×10^{-3} M. Each of these solutions were further incubated with benzene thiol ($[BT]_{final} = 10^{-5}$ to 10^{-13} M) for 12 h before substrate deposition. Next, to achieve high particle densities and aggregates, the samples were directly drop-cast (10 μL) on silicon wafers (0.5 × 0.5 cm). To achieve lower particle densities of approx. 5 and 50 particles × μm^{-2}, 10 μL (10^{-6} M in gold) of NPs were diluted in ethanol and spin-coated ((1st ramp) 500 rpm, 10 s; (2nd ramp) 3000 rpm, 30 s, with an acceleration rate for both ramps of 500 rpm per s) on silicon wafers (0.5 × 0.5 cm).

Characterization

UV-vis-NIR spectra were obtained using a Hewlett-Packard HP8453 spectrophotometer. Size, shape and topographical characterization of the nanoparticles and the substrates were performed by transmission and scanning electron microscopy (TEM, LEO 922 EFTEM operating at 80 kV, TEM, JEOL JEM 1010 operating at 100 kV and a LEO 1530 FE-SEM, Zeiss). SERS spectra were recorded in backscattering geometry with a Renishaw inVia Reflex system equipped with a 2D-CCD detector and a Leica confocal microscope. Excitation of the sample was carried out with a 785 nm laser line with acquisition times ranging from 0.5 to 10 s and power of about 0.15 and 3 mW in the sample. The laser was focused onto the sample with either a ×100 or ×50 objective, providing a spatial resolution of *ca.* 0.5–1 μm.

Conflicts of interest

There are no conflicts to declare.

Acknowledgements

N. P.-P., L. G., and M. A. C.-D. thank the MINECO-Spain (CTM2014-58481R, CTM2017-84050R, CTQ2017-88648R and RYC-2015-19107), Xunta de Galicia (Centro Singular de Investigacion de Galicia, Acc. 2016-19 and EM2014/035), Generalitat de Cataluña (2017SGR883), URV (2017PFR-URV_B2-02), URV and Banco Santander (2017EXIT-08) and the European Union (ERDF). This project has received funding from the European Union's Horizon 2020 research and innovation program under the MarieSkłodowska-Curie grant agreement No. 713679 and from the Universitat Rovira i Virgili. X. X. acknowledges the Lee Family Scholarship.

Notes and references

1 R. Alvarez-Puebla, L. M. Liz-Marzán and F. J. García de Abajo, *J. Phys. Chem. Lett.*, 2010, **1**, 2428–2434.
2 M. Sivis, N. Pazos-Perez, R. Yu, R. Alvarez-Puebla, F. J. García de Abajo and C. Ropers, *Commun. Phys.*, 2018, **1**, 13.
3 J. Ziegler, C. Wörister, C. Vidal, C. Hrelescu and T. A. Klar, *ACS Photonics*, 2016, **3**, 919–923.
4 B. Munkhbat, H. Pöhl, P. Denk, T. A. Klar, M. C. Scharber and C. Hrelescu, *Adv. Opt. Mater.*, 2016, **4**, 772–781.
5 R. T. Ginting, S. Kaur, D. K. Lim, J. M. Kim, J. H. Lee, S. H. Lee and J. W. Kang, *ACS Appl. Mater. Interfaces*, 2017, **9**, 36111–36118.
6 H. Yuan, Y. Liu, A. M. Fales, Y. L. Li, J. Liu and T. Vo-Dinh, *Anal. Chem.*, 2013, **85**, 208–212.
7 L. Rodríguez-Lorenzo, Z. Krpetic, S. Barbosa, R. A. Alvarez-Puebla, L. M. Liz-Marzán, I. A. Prior and M. Brust, *Integr. Biol.*, 2011, **3**, 922–926.
8 Y. Tian, Y. Zhang, Z. Teng, W. Tian, S. Luo, X. Kong, X. Su, Y. Tang, S. Wang and G. Lu, *ACS Appl. Mater. Interfaces*, 2017, **9**, 2114–2122.
9 A. M. Smith, M. C. Mancini and S. Nie, *Nat. Nanotechnol.*, 2009, **4**, 710–711.
10 A. Espinosa, J. Kolosnjaj-Tabi, A. Abou-Hassan, A. Plan Sangnier, A. Curcio, A. K. A. Silva, R. Di Corato, S. Neveu, T. Pellegrino, L. M. Liz-Marzán and C. Wilhelm, *Adv. Funct. Mater.*, 2018, **28**, 1803660.
11 K. Dong, Z. Liu, Z. Li, J. Ren and X. Qu, *Adv. Mater.*, 2013, **25**, 4452–4458.
12 R. Vankayala and K. C. Hwang, *Adv. Mater.*, 2018, **30**, 1706320.
13 C. Carrillo-Carrión, R. Martínez, M. F. Navarro-Poupard, B. Pelaz, E. Polo, A. Arenas-Vivo, A. Olgiati, P. Taboada, M. G. Soliman, Ú. Catalán, S. Fernández-Castillejo, R. Solà, W. J. Parak, P. Horcajada, R. A. Alvarez-Puebla and P. del Pino, *Angew. Chem., Int. Ed.*, 2019, **58**, 7078–7082.
14 Q. Jin, M. Li, B. Polat, S. K. Paidi, A. Dai, A. Zhang, J. V. Pagaduan, I. Barman and D. H. Gracias, *Angew. Chem., Int. Ed.*, 2017, **56**, 3822–3826.
15 K. S. B. Culver, Y. J. Shin, M. W. Rotz, T. J. Meade, M. C. Hersam and T. W. Odom, *J. Phys. Chem. C*, 2016, **120**, 22103–22109.
16 X. Deng, S. Liang, X. Cai, S. Huang, Z. Cheng, Y. Shi, M. Pang, P. A. Ma and J. Lin, *Nano Lett.*, 2019, **19**, 6772–6780.
17 S. K. Dondapati, T. K. Sau, C. Hrelescu, T. A. Klar, F. D. Stefani and J. Feldmann, *ACS Nano*, 2010, **4**, 6318–6322.
18 L. Rodríguez-Lorenzo, R. de la Rica, R. A. Álvarez-Puebla, L. M. Liz-Marzán and M. M. Stevens, *Nat. Mater.*, 2018, **17**, 205.
19 I. G. Theodorou, P. Ruenraroengsak, D. A. Gonzalez-Carter, Q. Jiang, E. Yagüe, E. O. Aboagye, R. C. Coombes, A. E. Porter, M. P. Ryan and F. Xie, *Nanoscale*, 2019, **11**, 2079–2088.
20 L. Zhou, K. J. Chen, J. D. Ramsey, C. K. Almlie and S. M. Burrows, *J. Phys. Chem. C*, 2018, **122**, 19823–19830.
21 S. Schlücker, *Angew. Chem., Int. Ed.*, 2014, **53**, 4756–4795.
22 A. S. D. S. Indrasekara, S. Meyers, S. Shubeita, L. C. Feldman, T. Gustafsson and L. Fabris, *Nanoscale*, 2014, **6**, 8891–8899.
23 L. Rodríguez-Lorenzo, R. A. Álvarez-Puebla, I. Pastoriza-Santos, S. Mazzucco, O. Stéphan, M. Kociak, L. M. Liz-Marzán and F. J. García de Abajo, *J. Am. Chem. Soc.*, 2009, **131**, 4616–4618.
24 L. Rodríguez-Lorenzo, R. A. Álvarez-Puebla, F. J. G. De Abajo and L. M. Liz-Marzán, *J. Phys. Chem. C*, 2010, **114**, 7336–7340.
25 M. Mueller, M. Tebbe, D. V. Andreeva, M. Karg, R. A. Alvarez-Puebla, N. Pazos-Perez and A. Fery, *Langmuir*, 2012, **28**, 9168–9173.
26 A. M. Fales, H. Yuan and T. Vo-Dinh, *Langmuir*, 2011, **27**, 12186–12190.
27 B. Mir-Simon, I. Reche-Perez, L. Guerrini, N. Pazos-Perez and R. A. Alvarez-Puebla, *Chem. Mater.*, 2015, **27**, 950–958.
28 D. Jimenez De Aberasturi, A. B. Serrano-Montes, J. Langer, M. Henriksen-Lacey, W. J. Parak and L. M. Liz-Marzán, *Chem. Mater.*, 2016, **28**, 6779–6790.
29 N. G. Bastús, J. Comenge and V. Puntes, *Langmuir*, 2011, **27**, 11098–11105.
30 K. B. Biggs, J. P. Camden, J. N. Anker and R. P. V. Duyne, *J. Phys. Chem. A*, 2009, **113**, 4581–4586.
31 H. Xu, J. Aizpurua, M. Käll and P. Apell, *Phys. Rev. E: Stat. Phys., Plasmas, Fluids, Relat. Interdiscip. Top.*, 2000, **62**, 4318–4324.
32 D. M. Solís, J. M. Taboada, F. Obelleiro, L. M. Liz-Marzán and F. J. García De Abajo, *ACS Nano*, 2014, **8**, 7559–7570.
33 X.-J. Wu and D. Xu, *Adv. Mater.*, 2010, **22**, 1516–1520.
34 R. Purbia and S. Paria, *Nanoscale*, 2015, **7**, 19789–19873.

35 S. Wang, M. Zhang and W. Zhang, *ACS Catal.*, 2011, **1**, 207–211.
36 A. Sousa-Castillo, L. N. Furini, B. D. B. Tiu, P. F. Cao, B. Topçu, M. Comesaña-Hermo, B. Rodríguez-González, W. Baaziz, O. Ersen, R. C. Advincula, M. Pérez-Lorenzo and M. A. Correa-Duarte, *Adv. Mater.*, 2018, **30**, 1707598.
37 P. Destito, A. Sousa-Castillo, J. R. Couceiro, F. López, M. A. Correa-Duarte and J. L. Mascareñas, *Chem. Sci.*, 2019, **10**, 2598–2603.
38 M. Sanles-Sobrido, W. Exner, L. Rodríguez-Lorenzo, B. Rodríguez-González, M. A. Correa-Duarte, R. A. Álvarez-Puebla and L. M. Liz-Marzán, *J. Am. Chem. Soc.*, 2009, **131**, 2699–2705.
39 C. Vázquez-Vázquez, B. Vaz, V. Giannini, M. Pérez-Lorenzo, R. A. Alvarez-Puebla and M. A. Correa-Duarte, *J. Am. Chem. Soc.*, 2013, **135**, 13616–13619.
40 P. Rivera_Gil, C. Vazquez-Vazquez, V. Giannini, M. P. Callao, W. J. Parak, M. A. Correa-Duarte and R. A. Alvarez-Puebla, *Angew. Chem., Int. Ed.*, 2013, **52**, 13694–13698.
41 A. Mariño-Lopez, A. Sousa-Castillo, M. Blanco-Formoso, L. N. Furini, L. Rodríguez-Lorenzo, N. Pazos-Perez, L. Guerrini, M. Pérez-Lorenzo, M. A. Correa-Duarte and R. A. Alvarez-Puebla, *ChemNanoMat*, 2019, **5**, 46–50.
42 N. Pazos-Perez, L. Guerrini and R. A. Alvarez-Puebla, *ACS Omega*, 2018, **3**, 17173–17179.
43 P. Aldeanueva-Potel, E. Carbó-Argibay, N. Pazos-Pérez, S. Barbosa, I. Pastoriza-Santos, R. A. Alvarez-Puebla and L. M. Liz-Marzán, *ChemPhysChem*, 2012, **13**, 2561–2565.
44 Y. Yang, J. Singh and M. Ruths, *RSC Adv.*, 2014, **4**, 18801–18810.
45 J. Turkevich, P. C. Stevenson and J. Hillier, *Discuss. Faraday Soc.*, 1951, **11**, 55–75.
46 W. Stöber, A. Fink and E. Bohn, *J. Colloid Interface Sci.*, 1968, **26**, 62–69.